

## Marginal Sea Overflows and the Upper Ocean Interaction

SHINICHIRO KIDA\*

*MIT/WHOI Joint Program, Woods Hole, Massachusetts*

JIAYAN YANG AND JAMES F. PRICE

*Woods Hole Oceanographic Institution, Woods Hole, Massachusetts*

(Manuscript received 11 October 2007, in final form 30 June 2008)

### ABSTRACT

Marginal sea overflows and the overlying upper ocean are coupled in the vertical by two distinct mechanisms—by an interfacial mass flux from the upper ocean to the overflow layer that accompanies entrainment and by a divergent eddy flux associated with baroclinic instability. Because both mechanisms tend to be localized in space, the resulting upper ocean circulation can be characterized as a  $\beta$  plume for which the relevant background potential vorticity is set by the slope of the topography, that is, a topographic  $\beta$  plume.

The entrainment-driven topographic  $\beta$  plume consists of a single gyre that is aligned along isobaths. The circulation is cyclonic within the upper ocean (water columns are stretched). The transport within one branch of the topographic  $\beta$  plume may exceed the entrainment flux by a factor of 2 or more.

Overflows are likely to be baroclinically unstable, especially near the strait. This creates eddy variability in both the upper ocean and overflow layers and a flux of momentum and energy in the vertical. In the time mean, the eddies accompanying baroclinic instability set up a double-gyre circulation in the upper ocean, an eddy-driven topographic  $\beta$  plume. In regions where baroclinic instability is growing, the momentum flux from the overflow into the upper ocean acts as a drag on the overflow and causes the overflow to descend the slope at a steeper angle than what would arise from bottom friction alone.

Numerical model experiments suggest that the Faroe Bank Channel overflow should be the most prominent example of an eddy-driven topographic  $\beta$  plume and that the resulting upper-layer transport should be comparable to that of the overflow. The overflow-layer eddies that accompany baroclinic instability are analogous to those observed in moored array data. In contrast, the upper layer of the Mediterranean overflow is likely to be dominated more by an entrainment-driven topographic  $\beta$  plume. The difference arises because entrainment occurs at a much shallower location for the Mediterranean case and the background potential vorticity gradient of the upper ocean is much larger.

### 1. Overflow and upper ocean interaction

Marginal sea overflows enter the open ocean as dense, bottom-trapped gravity currents (Fig. 1). The Denmark Strait, Faroe Bank Channel, Mediterranean Sea, Red Sea, and Filchner Bank overflows are five major marginal sea overflows that are known to play an important role in supplying deep and intermediate water masses to

the global ocean (Warren 1981). Observations indicate that overflows also affect their overlying water through entrainment and eddy formation (Saunders 2001; Candela 2001, and references therein).

#### *a. Mass and vorticity balances*

The importance of overflows on determining the deep ocean properties led past studies to focus on how entrainment affects overflows. Understanding how the dynamics of overflows evolve as they descend the continental slope progressed from so-called stream-tube models (e.g., Smith 1975; Killworth 1977; Price and Baringer 1994). Stream-tube models assume an inactive upper layer, which may have been appropriate to explain the basic dynamics of the overflow. However, this assumption certainly cannot be appropriate for the

---

\* Current affiliation: Earth Simulator Center, Japan Agency for Marine-Earth Science and Technology, Yokohama, Japan.

---

Corresponding author address: ESC, JAMSTEC, 3173-25 Showa-machi, Kanazawa-ku, Yokohama 236-0001; Japan.  
E-mail: Kidas@jamstec.go.jp

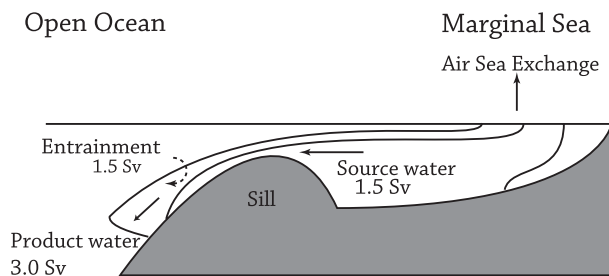


FIG. 1. Schematic of an overflow and its mass balance: The transport values are roughly based on the Faroe Bank Channel overflow. Dense water that forms in the marginal sea spills over the sill as an overflow. This overflow (1.5 Sv) descends the continental slope, entrains overlying upper oceanic water (1.5 Sv), and reaches its neutral buoyancy level or the bottom. Figure adapted from Price and Baringer (1994).

upper oceanic layer because the upper ocean also needs to balance mass lost to the overflow somehow. The Faroe Bank Channel overflow, for example, entrains about 1.5 Sv ( $\text{Sv} \equiv 10^6 \text{ m}^3 \text{ s}^{-1}$ ) of overlying North Atlantic water near the shelf break while descending the continental slope (Fig. 1) (Mauritzen et al. 2005). Localized entrainment also implies vortex stretching in the upper ocean. So, there must be a convergent flow in the upper ocean that balances both the mass and vorticity fluxes induced by entrainment.

#### b. Time variability associated with overflows

Satellite altimetry revealed regions of high variability of the sea surface height about 50–100 km downstream from the marginal sea strait of the Mediterranean, Faroe Bank Channel, and Denmark Strait overflows (Høyer and Quadfasel 2001; Høyer et al. 2002). Satellite infrared imagery and floats have also shown intense cyclones forming above the Denmark Strait overflow, suggesting active upper ocean and overflow interaction (Bruce 1995; Krauss and Käse 1998). For the Faroe Bank case, which we will emphasize here, snapshots of sea surface height show fluctuations of  $\pm 10$  cm and eddies having a radius of roughly 50 km (Ezer 2006). In situ observations of the overflow show the corresponding mass and current variability: the temperature of the Faroe Bank Channel overflow has been observed to fluctuate with a 3–4-day period about 140 km downstream from the Faroe Bank Channel (Fig. 2; Høyer and Quadfasel 2001; Geyer et al. 2006). These latter observations appear to show more or less discrete eddies moving along the bathymetry. At a given point, the associated temperature fluctuations are up to  $4^\circ\text{C}$ , comparable to the temperature difference between the Faroe Bank Channel source water and the ambient North Atlantic water (Mauritzen et al. 2005). The

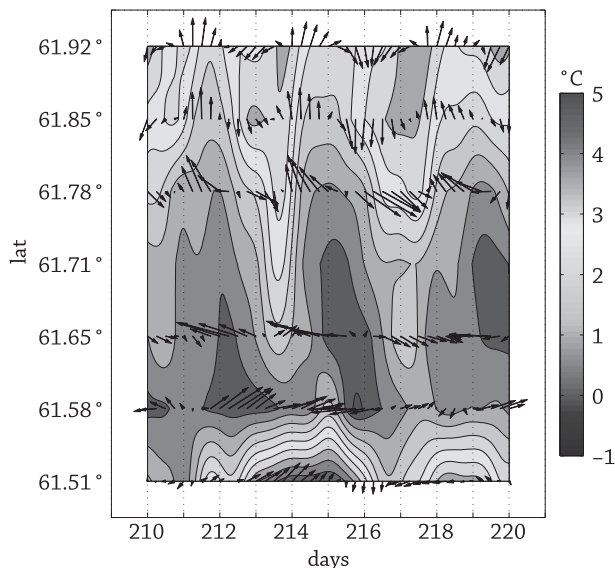


FIG. 2. Time–latitude plot of the near-bottom temperatures (contoured) and bandpassed (2–8 days) currents (arrows) of the Faroe Bank Channel overflow observed about 140 km downstream from the Faroe Bank Channel (Høyer and Quadfasel 2001). The temperature fluctuates with a 3–4-day period. Figure reproduced by courtesy of D. Quadfasel.

temperature of the Mediterranean overflow has also been observed to fluctuate with a 7–9-day period about 200 km downstream from the Strait of Gibraltar with no such oscillations observed near the strait (Stanton 1983; Chérubin et al. 2003). The Denmark Strait overflow has also been observed to be associated with significant time variability (Käse et al. 2003). Observations indicate large time variability both in the overflow layer and its overlying oceanic layer downstream from the strait.

There has been some progress in understanding the time variability associated with overflows and its generation mechanisms. Laboratory experiments have shown steady and laminar overflows developing variability, such as waves and eddies downstream from straits (Cenedese et al. 2004). Multiple regimes of eddy formation associated with strong cyclones and anticyclones in the upper layer have also been found (e.g., Whitehead et al. 1990; Etling et al. 2000). Primitive equation models support development of such variability downstream from the strait as a result of interaction with its upper layer through entrainment, baroclinic instability, and vortex stretching (Jiang and Garwood 1996; Spall and Price 1998; Jungclaus et al. 2001). One-and-a-half-layer models of overflows, however, have also shown that overflows may become a chain of eddies even in the absence of upper-layer motion when the transport of the source water varies with time (Nof 1991) or when a steady solution does not exist for the overflow layer

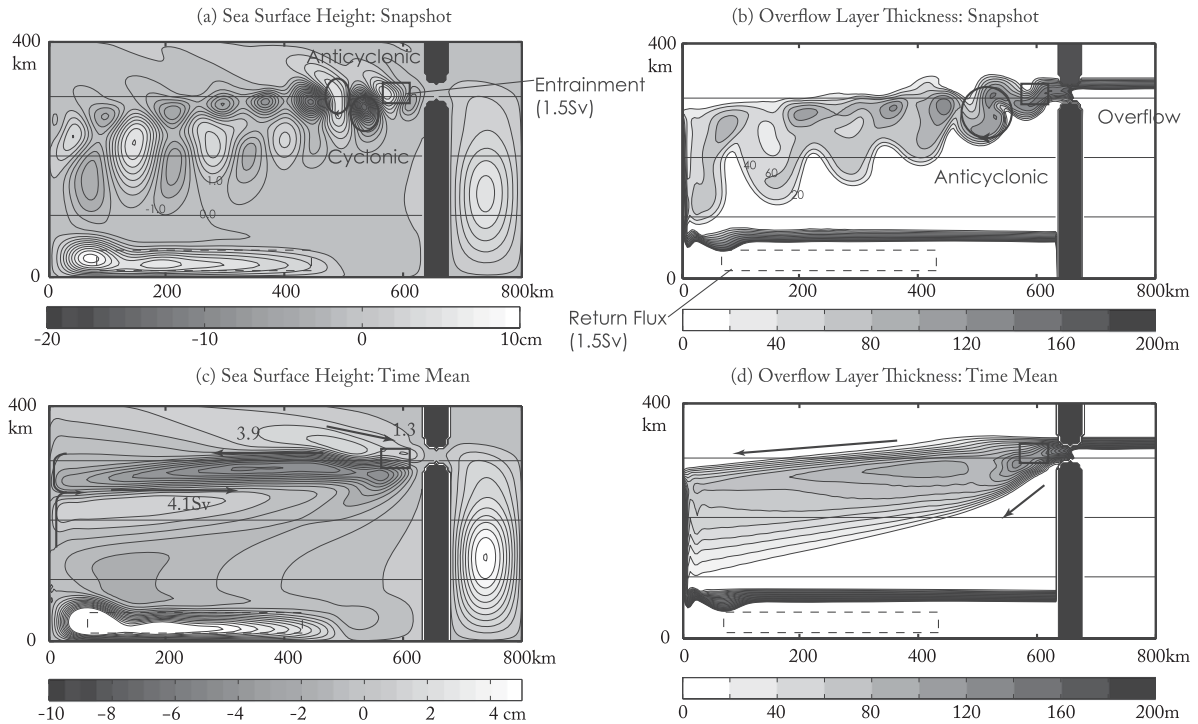


FIG. 3. (top) A snapshot and (bottom) time-mean flow fields for Case 1: The marginal sea is located on the eastern side of the domain and the continental slope region is located to the west. Straight black solid lines are the bathymetric contours representing  $-3000$ ,  $-2000$ , and  $-1000$  m. The white solid-squared region near the strait is the prescribed entrainment region. (a) A snapshot of the sea surface height contoured every  $1$  cm: Eddies of both signs are observed with a sea surface height of  $\pm 15$  cm, radius of  $50$  km, and azimuthal velocity of  $40$   $\text{cm s}^{-1}$ . The cyclonic eddies appear to outnumber the anticyclonic eddies. (b) A snapshot of the overflow layer thickness contoured every  $20$  m. The overflow layer repeatedly forms an anticyclonic eddy near the strait, which then detaches and propagates along the bathymetric contours while slowly descending the slope. (c) The time-mean sea surface height contoured every  $0.5$  cm. The major feature is a cyclonic circulation aligned approximately with the bathymetric contours with a transport of  $4.5$  Sv. A smaller double-gyre structure is also observed near the strait. The transport of the anticyclonic gyre is  $2.0$  Sv. (d) The time-mean overflow layer thickness contoured every  $20$  m. Notice that the overflow descends sharply near the strait but descends gradually away from the strait.

(Nof et al. 2002), suggesting that not all eddy generation mechanisms are a result of overflow–upper ocean interaction. While various eddy generation mechanisms may coexist, past studies strongly suggest that the upper oceanic layer is affected by eddies induced by overflows.

### c. Modeling the overflow and its overlying ocean (Case 1)

How is the upper oceanic layer balancing the mass lost to the overflow layer? What is the impact of eddies observed in the overflow and upper oceanic layers on the time-mean flow? Past studies have primarily focused on the instantaneous overflow–upper ocean interaction, and its impact on the time-mean flow has not been much investigated. To learn how a marginal sea overflow may interact with the upper ocean, we have constructed a two-layer isopycnal model representing the overflow and its overlying ocean. The parameter space is set close to that of the Faroe Bank Channel overflow (model specifics will be described in the next section). The so-

lution shows a highly time-varying flow field that is dominated by eddies (Figs. 3a and 3b). The dominant fluctuation period in the upper ocean is  $4$ – $5$  days, the same as in the overflow layer, which we believe is analogous to the time variability observed near the Faroe Bank Channel overflow (Fig. 2) (Høyer and Quadfasel 2001). A significant time-mean circulation forms in the upper oceanic layer (Fig. 3c); there is cyclonic circulation, more or less aligned along the bathymetric contours, that has a transport of  $5.4$  Sv. There is a smaller anticyclonic circulation near the strait having a transport of about  $1.0$  Sv. This experiment, referred to as Case 1, indicates that the overflow–upper ocean interaction leads to establishment of a significant time-mean flow and that the eddy variability likely plays a major role in its dynamics.

### d. The goal and the outline

The goal of this paper is to understand how a marginal sea overflow may interact with the upper ocean and, so,

explain the flow field of Case 1, which we believe has some relevance to the real ocean. Outstanding questions are as follows:

- 1) How does the upper ocean balance the mass lost to the overflow?
- 2) What is the primary mechanism for the formation of the eddies observed in the overflow and its overlying oceanic layers?
- 3) Do eddies have a significant impact on the overflow and its overlying oceanic layers in the time mean?

We will address these three questions by using the comparatively simple and idealized ocean model (simple compared to a full GCM) used for Case 1. The details of this idealized ocean model are described in section 2. The first question is examined very briefly in section 3 since this largely repeats an earlier study (Kida et al. 2008). The second and third questions are examined in detail in sections 4 and 5. The concept of a  $\beta$  plume will be used extensively for examining the overflow–upper ocean interaction, and the notion of an eddy-driven topographic  $\beta$  plume is introduced in section 4. Summary and remarks will be presented in the final section.

## 2. The two-layer isopycnal model

The numerical ocean model used for Case 1 is a two-layer isopycnal model derived by making small changes from the Hallberg Isopycnal Model (Hallberg 1997). For this study, the external parameters are chosen to mimic the Faroe Bank Channel overflow (Figs. 4a and 4b) (Borenäs and Lundberg 2004). The Faroe Bank Channel was chosen for the base case primarily because it is one of the better-observed major overflows. The two layers represent the overflow and its overlying oceanic layers with a density difference of  $0.5 \text{ kg m}^{-3}$ , which represents the density difference after entrainment (Mauritzen et al. 2005). The Coriolis parameter is set to a constant,  $f = 1.4 \times 10^{-4} \text{ s}^{-1}$ , and the domain is  $800 \text{ km}$  long in the along-slope direction and  $400 \text{ km}$  long in the cross-slope direction. The spatial resolution is  $4 \text{ km}$ . The model domain is separated into two basins: The smaller (eastern) basin represents the marginal sea and the larger (western) basin represents the continental slope region and open ocean (Fig. 4b). The strait connecting the two basins is  $16 \text{ km}$  wide and  $1000 \text{ m}$  deep at the narrowest point of the strait. The bottom bathymetry in the two basins and the strait has a slope of  $0.01$  with a shallower region to the north, so the initial potential vorticity (PV) contours run through the strait.

A circulation is forced by pumping  $1.5 \text{ Sv}$  of mass into the overflow layer within the marginal sea and by

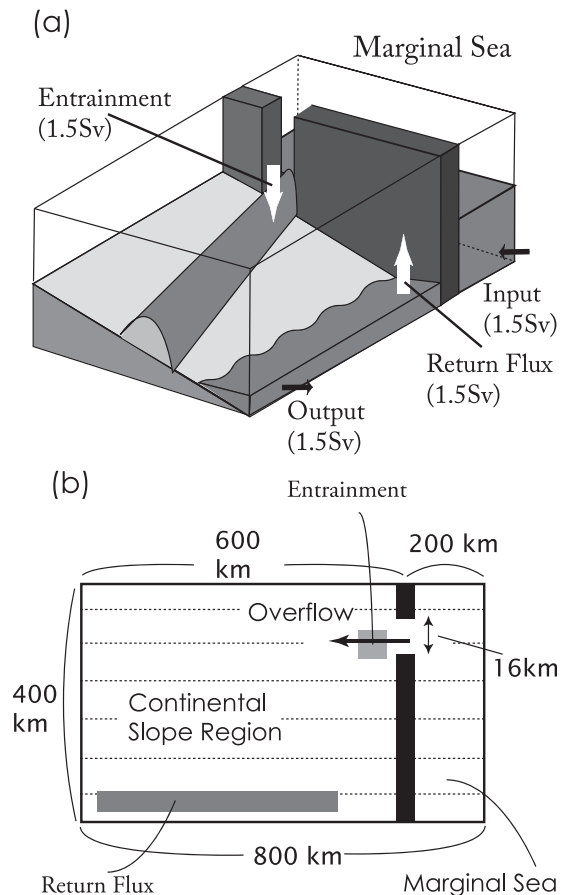


FIG. 4. Schematic of the model configuration for Case 1. (a) 3D view and (b) bird's-eye view: The domain,  $800 \text{ km} \times 400 \text{ km}$ , has two basins connected by a narrow strait  $16 \text{ km}$  wide and  $1000 \text{ m}$  deep. The smaller basin represents the marginal sea and the larger basin represents the continental slope/open ocean region. The bottom topography in both basins and the strait has a slope of  $0.01$ . To create an overflow at the strait, mass is pumped into the overflow layer in the marginal sea and an equivalent amount of mass is pumped out of the slope region to conserve mass. Note that this mass forcing is applied only to the overflow layer. Entrainment is prescribed to occur near the strait (light-shaded region) with a return flux from the overflow to the upper layer located offshore to balance mass (dark-shaded region).

pumping an equivalent amount of mass out of the lower layer in the offshore region. Thus mass is conserved in both layers. Entrainment, that is, a diapycnal mass flux from the upper layer and into the lower layer, is prescribed in a region near the strait:  $20\text{--}80 \text{ km}$  from the strait, between  $600$  and  $920 \text{ m}$ , and with a uniform diapycnal velocity ( $w^* = 1.6 \times 10^{-3} \text{ m s}^{-1}$ ). This gives a net transfer of  $1.5 \text{ Sv}$ , based upon the observational results of Mauritzen et al. (2005). The necessary return flux (overflow layer to the upper oceanic layer) is prescribed in the offshore region noted above; this is the present model's equivalent to the upwelling and diapycnal

mixing that likely occurs over a global scale in the real ocean. The return flux is located well offshore so that the presence of the strong PV gradient imposed by the slope inhibits direct influence of this return flux to the dynamics near the entrainment region. The dynamics near the entrainment region do not differ significantly from experiments where the return flux is located much farther offshore. Note that the upper layer is not forced to create a flow from the open ocean to the marginal seas that would counter the overflow at the strait. The upper oceanic layer is forced only by entrainment or interfacial pressure work that occurs between the overflow. This is to isolate the impact of overflow on the upper ocean layer.

Linear drag (bottom friction,  $\nu = 1.5 \times 10^{-5} \text{ s}^{-1}$ ) and biharmonic viscosity ( $A_{H4} = -8 \times 10^8 \text{ m}^4 \text{ s}^{-1}$ ) are used for frictional dissipation. Bottom friction acts only on the layer that directly contacts the bottom bathymetry.

Our model configuration is similar to what is known as Dynamics of Overflow Mixing and Entrainment (DOME) configuration (Ezer and Mellor 2004; Ezer 2005; Legg et al. 2006), and we will compare our results to those using the DOME setup in various parts of this paper. However, there are some differences between the two model configurations. The most significant difference is that the overflow enters the open ocean from the marginal sea following the geostrophic contours in our model, while overflows in the DOME setup do not. Overflows in DOME are tipped off the shelf initially, flow across bathymetry lines, and experience geostrophic adjustment. Entrainment is also prescribed in our model, but DOME does not. While the DOME setup has various aspects close to reality, it is at the same time hard to isolate various processes occurring to overflows. Our model is intended to focus more on the dynamics of overflows after initial geostrophic adjustment has taken place.

### 3. Entrainment-driven topographic $\beta$ plume (Case 2)

The flow field of Case 1 is fairly complicated (Figs. 3a–d), either in a snapshot or in the mean. To understand how this flow field was established, we will examine the role of each process in the model separately. First, the overflow layer will be neglected and the upper oceanic response to localized entrainment is examined. This experiment will be referred to as Case 2. The two-layer isopycnal model described above is then reduced to a one-layer model and entrainment/detrainment is equivalent to a mass sink/source.

The upper oceanic layer responds to entrainment by forming a steady cyclonic circulation with a transport of

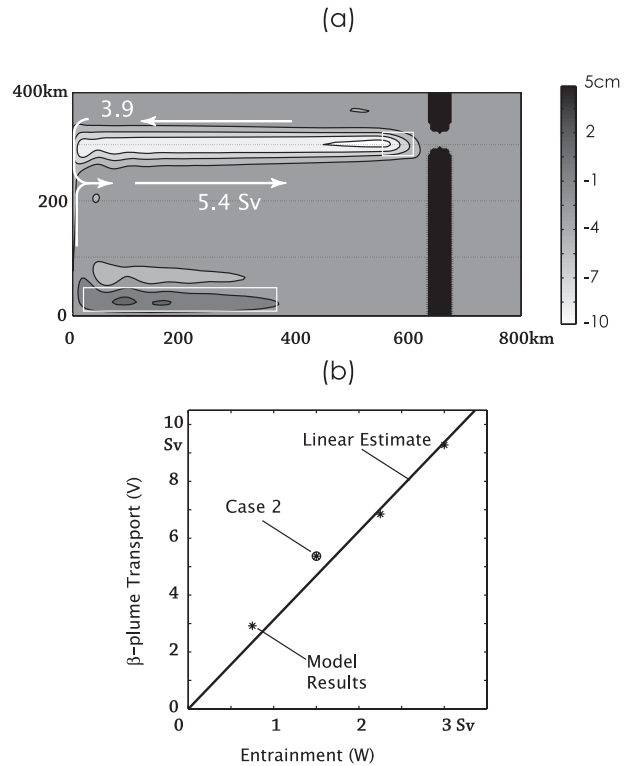


FIG. 5. (a) Sea surface height for Case 2, contoured every 1 cm. An entrainment-driven topographic  $\beta$  plume with a transport of 5.4 Sv forms within the upper oceanic layer. (b) The topographic  $\beta$ -plume transport as the strength of entrainment ( $W$ ) is varied. The asterisks show the model results (for Case 2 shown with a circle) and indicate that Eq. (1) gives a good estimate for the topographic  $\beta$ -plume transport found in the numerical model.

5.0 Sv (Fig. 5a). This circulation is well described as a  $\beta$  plume (Stommel 1982; Spall 2000) and its transport ( $V$ ) can be estimated as

$$V = \frac{fW}{\beta^* L_y}, \quad (1)$$

where  $W$  is the total diapycnal transport,  $L_y$  is the length of the entrainment region across the slope, and  $\beta^*$  is the topographic  $\beta$ , which is  $f\alpha/H$  with  $\alpha$  as the slope and  $H$  the mean upper-layer thickness. The basic parameter space for the Faroe Bank Channel overflow includes  $f = 1.4 \times 10^{-4} \text{ s}^{-1}$ ,  $L_y = 30 \text{ km}$ ,  $\alpha = 0.01$ ,  $H = 1000 \text{ m}$ , so Eq. (1) estimates the transport of the topographic  $\beta$  plume to be 5.4 Sv, which is very close to what the model flow field shows. Equation (1) gives excellent estimates of the transport of the topographic  $\beta$  plume even when the strength of the entrainment is varied widely (Fig. 5b). This entrainment-forced topographic  $\beta$  plume remains steady (little or no eddy variability) within a parameter range that is close to that of the Faroe Bank Channel. In a one-layer model where baroclinic

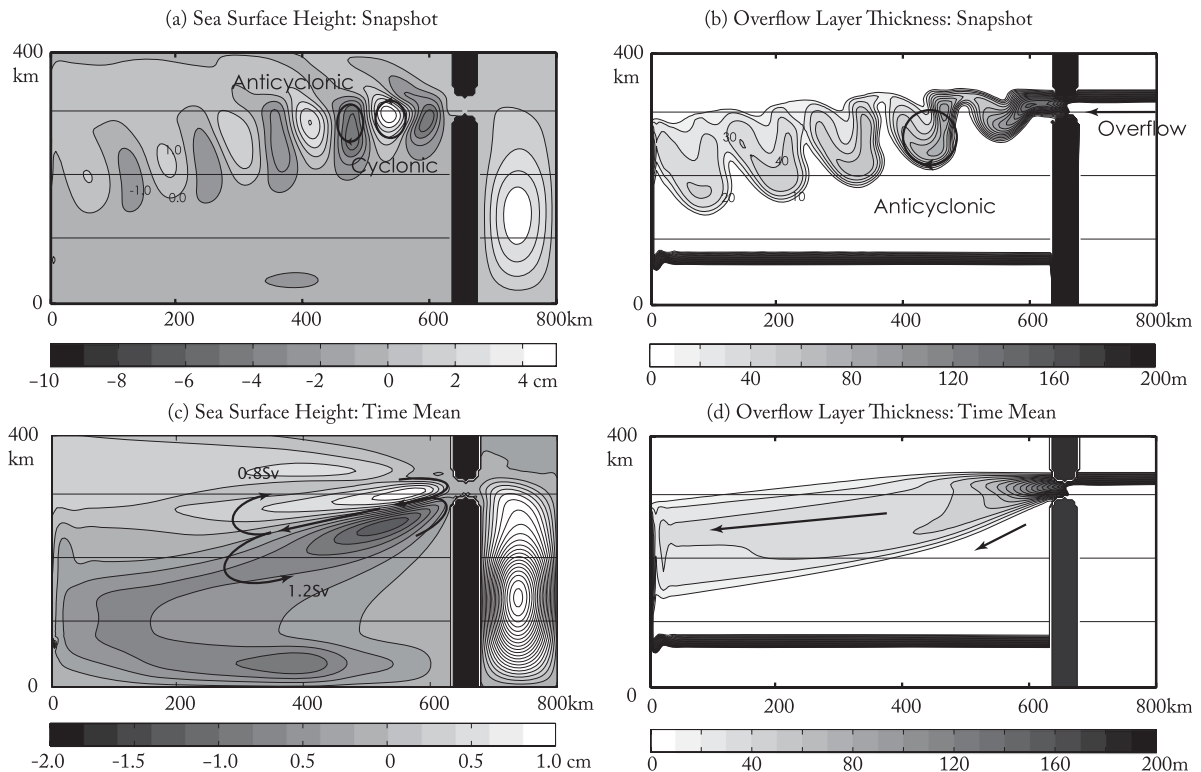


FIG. 6. A snapshot and the time-mean flow fields for Case 3: (a) Snapshot of the sea surface height contoured every 1 cm. Eddies of both signs are observed with a radius of 30 km, sea surface height of  $\pm 10$  cm, and azimuthal velocity of  $30 \text{ cm s}^{-1}$ . (b) Snapshot of the overflow layer thickness contoured every 10 m. The overflow forms into an anticyclonic eddy with a radius of 50 km roughly every 5 days and flows roughly along the continental slope. The eddies gradually become a thin wavy layer as they travel farther away from the strait. (c) The time-mean sea surface height contoured every 0.2 cm. An eddy-driven  $\beta$  plume forms with two gyres rotating in opposite directions. The cyclonic gyre and the anticyclonic gyre have a transport of roughly 1.2 and 0.8 Sv, respectively. (d) The time-mean overflow layer thickness contoured every 10 m. The overflow descends more sharply near the strait than farther downstream.

instability is not possible, it is a safe conclusion that the entrainment-forced topographic  $\beta$  plume will not become unstable and create the intense eddy variability found in Case 1.

#### 4. The eddy-driven topographic $\beta$ plume (Case 3)

The possibility of an adiabatic overflow–upper ocean interaction will be examined in this section, which will be referred to as Case 3. The model used is similar to that of Case 2 except in two important ways: First, the prescribed entrainment is absent from the model so that there is no diabatic forcing between the two layers. Second, an overflow layer is induced by prescribing a dense water formation process in the marginal sea basin (Fig. 4). An active upper layer is present, so this is a two-layer model. Thus, the model used in Case 2 had entrainment and neglected the overflow layer, but the model used here in Case 3 has the overflow layer and neglects entrainment. The difference in the flow compared to Case 2 is striking; this model solution includes

vigorous baroclinic eddies that generate an upper-layer circulation that we term an eddy-driven topographic  $\beta$  plume.

##### a. The formation of eddies

Eddies form in the overflow layer and the upper oceanic layer (Figs. 6a and 6b). The snapshot of the sea surface height shows the formation of eddies with both signs, with a radius of 30 km, sea surface height of  $\pm 10$  cm, and an azimuthal velocity of  $30 \text{ cm s}^{-1}$  (Fig. 6a). The overflow layer thickness shows the overflow forming anticyclonic eddies (Fig. 6b). These anticyclonic eddies form roughly every 5 days with a radius of 50 km and are also observed farther downstream from the strait. Although these eddies are discrete, the mean overflow velocity is as fast as  $50 \text{ cm s}^{-1}$  and is dominantly in the westward ( $-x$ ) direction, so the absolute velocity within the overflow never reverses even in the presence of eddies. The velocity in the upper layer, instead, shows the absolute velocities changing signs with 4–6-day period because there is no such strong background flow.

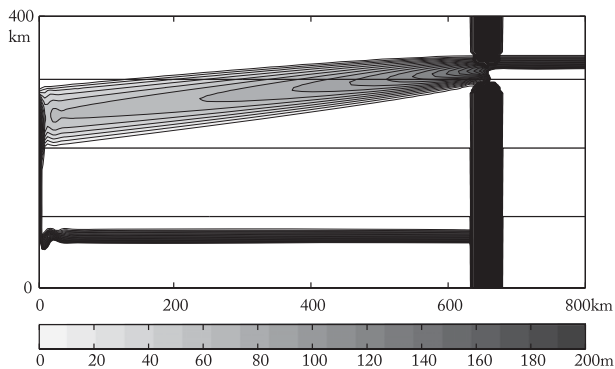


FIG. 7. A snapshot of the overflow layer when the upper layer thickness is 2000 m thicker than in Case 3: overflow layer thickness contoured every 10 m. No eddy formation occurs: Thus, the overflow remains steady and flows roughly along the geostrophic contours while descending according to the bottom Ekman number. Upper layer motion is absent: Thus no time-mean flow field is established.

*b. The mechanism for generating eddies*

The behavior of eddies, such as the location of eddy formation or the intensity of eddies observed at the surface and the overflow layer, changes when the external parameters of the model change. An extreme example is when the upper layer thickness ( $H$ ) is 2000 m thicker than the model used in Case 3. Then the overflow layer remains a steady stream-tube-like flow and no significant flow is induced in the upper layer, thus no establishment of the eddy-driven topographic  $\beta$  plume (Fig. 7). The velocity and thickness of the overflow layer at the strait is similar to that in Case 3, but the overflow layer now flows roughly along isobaths while descending the slope with an angle about that estimated from the bottom Ekman number ( $\nu/f$ ). A similar steady-state solution can be achieved when other parameters of the model are varied, but this extreme example suggests that an active upper layer is one of the important components for the eddies observed in Case 3 to form. In absence of upper-layer motion, the overflow appears to be stable. An eddy-generation mechanism based on  $1\frac{1}{2}$ -layer dynamics (Nof 1991; Nof et al. 2002) is therefore unlikely to be responsible for generating the eddies observed in Case 3.

A plausible mechanism for generating the eddies in Case 3 is baroclinic instability. Since the mean thickness of overflows is typically a parabolic shape in the cross-slope direction, the PV gradient in the cross-slope direction changes sign and the necessary condition for baroclinic instability is satisfied. The analytical solution for the growth rate of baroclinic instability derived by Swaters (1991) also gives a reasonable indication for when instability occurs in the model. Swaters (1991)

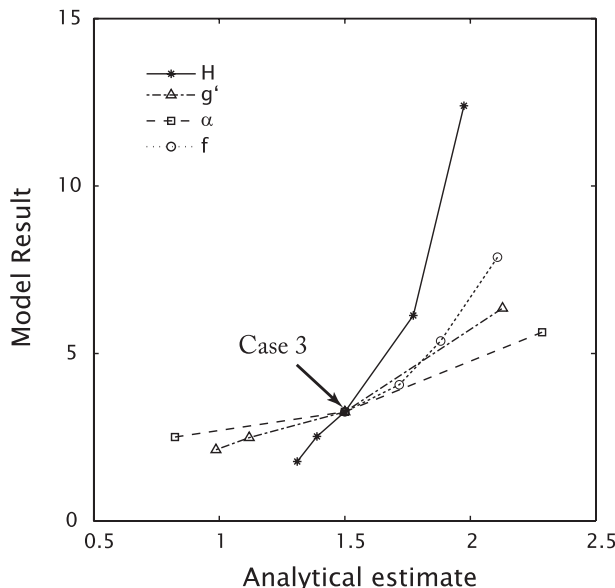


FIG. 8. The nondimensional distance required for instability, estimated using the analytical solution of Swaters (1991), plotted against the distance observed in the model. All cases show that the distance required for instability vary with  $H$ ,  $g'$ ,  $\alpha$ , and  $f$  according to the analytical solution. Note that each of the lines corresponds to cases in which only one parameter is varied from Case 3 and all other parameters are fixed. Values from the model are also nondimensionalized by  $L_D$ .

showed that  $\mu [ = (h_2/L_D)/\alpha$ , where  $h_2$  is the overflow thickness and  $L_D$  is the deformation radius of the upper layer], a nondimensional parameter comparing the thickness gradient of the overflow to the slope, is the main controlling parameter for the growth rate: larger  $\mu$  leading to a faster growth rate. Using their analytical solution for growth rate, the distance required for full growth of instability can be estimated, and these estimates are able to capture the parameter dependence of baroclinic instability well, although there were some differences with each parameter (Fig. 8). The analytical estimate and the model results do not exactly match, but this is likely because the analytical estimate is one based on linear perturbation, whereas the model values are results of finite amplitude instability. Note that the distance required for full growth of eddies is also sensitive to the linear drag coefficient  $\nu_o$ , which we kept constant in the model: larger  $\nu_o$  leads to longer distance. The size of the eddies observed in the model also matches with the wavelength that estimates the maximum growth rate of the instability, consistent with the results of Helfrich (2006). The dependence of eddy formation on  $\mu$  matches with the laboratory experiments of Cenedese et al. (2004). Cenedese et al. showed that eddies form when the Froude number is small, which corresponds to our model case when  $\mu$  is small

since  $\mu$  can be expressed using the Froude number as  $\mu = 1/\text{Fr}\sqrt{h_2/h_1}$  and can roughly be interpreted as inverse of the Froude number. Their wave regime did not occur in our model experiments, but this is likely because the Froude number of the overflow in our model does not exceed 1—a necessary condition for the wave regime.

The eddies observed in all of our model experiments consisted of both cyclones and anticyclones with roughly equal numbers. This is similar to past model experiments in which baroclinic instability was suggested as the likely generation mechanism of the eddies (e.g., Swaters 1991; Choboter and Swaters 2000; Jungclaus et al. 2001; Jiang and Garwood 1996). Preference on the sign of the eddies did not occur, unlike some previous studies in which a dominant formation of barotropic cyclones was observed (Spall and Price 1998; Etling et al. 2000). Etling et al. (2000) suggests that the formation of barotropic cyclones is in dynamically different regimes from baroclinic instability and that the barotropic cyclone regime can be expected when  $\mu$  is small. However, our model experiments do not form barotropic cyclones even when  $\mu$  is small, at least within the various parameter space that we tested, suggesting that  $\mu$  may not be the single parameter that distinguishes the two eddy regimes. We suspect that the difference between the two regimes is caused by the difference in the vertical structure of the overflow. The Denmark Strait overflow, which Spall and Price (1998) focused on, is a two-layer overflow (strong stratification within the overflow layer) and strong stretching occurs in the upper portion of the overflow as it descends the slope. This vortex stretching effect does not occur for a single-layer overflow that gradually thins and flattens. The PV dynamics of the water column is likely to be quite different between the baroclinic and barotropic eddy formation regimes.

### c. The time-mean flow field of the upper layer

The time-mean sea surface height shows the formation of a double-gyre, which we call the eddy-driven topographic  $\beta$  plume (Fig. 6c). The offshore cyclonic gyre and the onshore anticyclonic gyre have a transport of roughly 1.2 and 0.8 Sv, respectively, which is comparable to the overflow transport. This double-gyre structure is the major difference from the cyclonic entrainment-driven topographic  $\beta$  plume (Case 2).

#### WHY A DOUBLE GYRE?

Why are the eddies capable of inducing a double-gyre flow field in the upper oceanic layer? The processes can be revealed from the full vorticity equation of the upper oceanic layer:

$$\overline{\mathbf{U}}_1 \cdot \nabla \bar{q}_1 = \bar{q}w^* + \mathbf{k} \cdot \nabla \times \overline{\mathcal{F}}_1 - \nabla \cdot \overline{\mathbf{U}}_1 q_1', \quad (2)$$

where  $U$  is the transport,  $q$  is the PV,  $\mathcal{F}$  is friction, and overbars and primes represent the time mean and fluctuation, respectively, with subscript 1 used for the values in the upper layer. The mean background PV gradient  $\nabla \bar{q}_1$  is largely controlled by the slope:

$$\nabla \bar{q}_1 \simeq \left( \frac{q_1 \nabla h_b}{h_1} \right), \quad (3)$$

where  $h_1$  is the upper-layer thickness and  $h_b$  is the bottom topography, so the term on the lhs of Eq. (2) roughly represents the PV advection due to a flow across isobaths. The three terms on the rhs of Eq. (2) are PV forcing by entrainment ( $\bar{q}_1 w^*$ ), friction ( $\mathbf{k} \cdot \nabla \times \overline{\mathcal{F}}_1$ ), and eddy PV flux divergence ( $\nabla \cdot \overline{\mathbf{U}}_1 q_1'$ ).

The three terms on the rhs of Eq. (2) show the three processes that balance the lhs and thus induce a flow across isobaths. For Case 3, PV forcing by entrainment does not exist and dissipation is negligible in the interior, so the dominant term balancing the PV advection term near the strait is the eddy PV flux divergence term:

$$\overline{\mathbf{U}}_1 \cdot \nabla \bar{q}_1 \simeq -\nabla \cdot \overline{\mathbf{U}}_1 q_1'. \quad (4)$$

This balance is often termed as the turbulent Sverdrup balance (Haidvogel and Rhines 1983). The eddy PV flux divergence turns out to have two regions with different signs: An eddy PV flux convergence region and an eddy PV flux divergence region on its onshore side (not shown). Since the mean PV gradient of the upper layer is positive throughout the continental slope region, the two regions of eddy PV flux divergence with different signs will force a bidirectional time-mean flow across the PV gradient and give rise to the double-gyre structure of the eddy-driven topographic  $\beta$  plume as observed in the time-mean flow field (Fig. 6c).

But why are the eddies creating two regions of eddy PV flux divergence in the upper layer? To understand this, the eddy PV flux divergence term needs to be decomposed. Under the quasigeostrophic (QG) assumption (which is valid for the upper layer), the role of the eddy PV flux divergence can be divided into a Reynolds stress and a form drag (Rhines and Holland 1979; Plumb 1986):

$$\begin{aligned} & \nabla \cdot \overline{\mathbf{u}}_1' Q_1' \\ &= \frac{\partial}{\partial x} \left( \overline{u_1' \zeta_1'} - \frac{f \overline{u_1' h_1'}}{H} \right) + \frac{\partial}{\partial y} \left( \overline{v_1' \zeta_1'} - \frac{f \overline{v_1' h_1'}}{H} \right), \\ &= \nabla \cdot (\overline{u_1' \zeta_1'}, \overline{v_1' \zeta_1'}) + \nabla \cdot \left( -\frac{f \overline{u_1' h_1'}}{H}, -\frac{f \overline{v_1' h_1'}}{H} \right), \end{aligned} \quad (5)$$



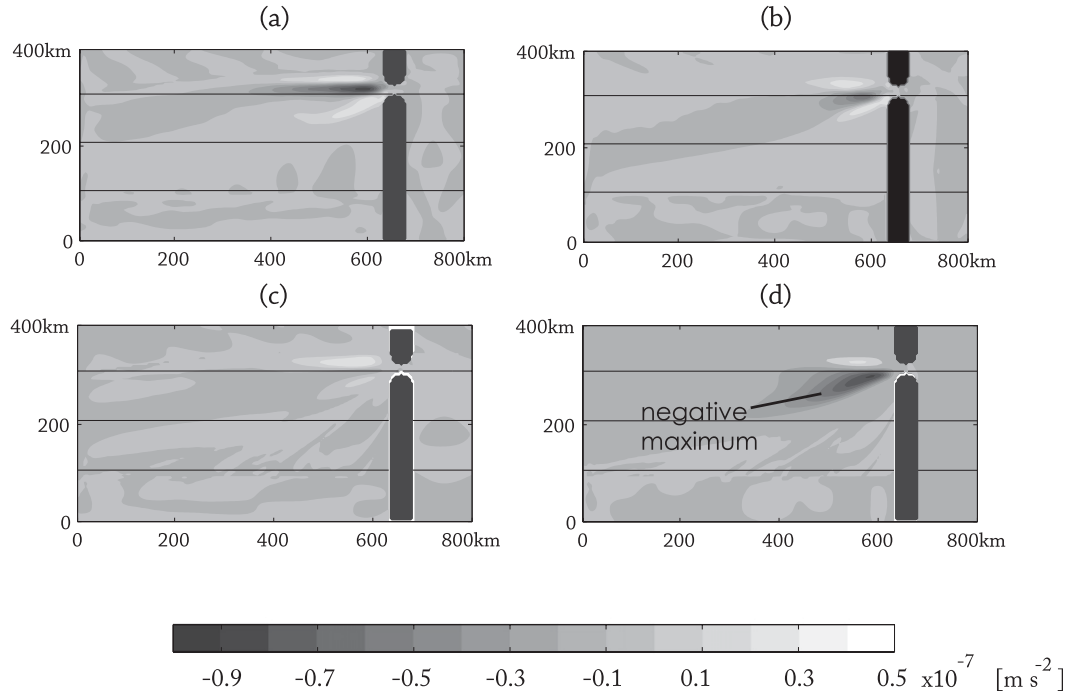


FIG. 9. Reynolds stress in (a) the  $x$  direction  $(\overline{u'_1 \zeta'_1})$  and (b)  $y$  direction  $(\overline{v'_1 \zeta'_1})$ . Form drag in (c)  $x$  direction  $(H^{-1} \overline{f u'_1 h'_1})$  (d)  $y$  direction  $(H^{-1} \overline{f v'_1 h'_1})$ . This is the largest term among other eddy PV flux terms, thus the dominant term deciding the structure of the eddy PV flux divergence.

where  $Q$  is the QGPV,  $\zeta$  is the relative vorticity, and  $u$  is the velocity. The first term represents the divergence of the Reynolds stress and the second term represents the divergence of the form drag. For Case 3, the  $y$  component (onshore direction) of the form drag is apparently the largest term with a negative maximum (Fig. 9). This result shows that momentum is fluxed from the overflow to the upper layer dominantly in this direction through form drag. As Eq. (5) shows, the negative maximum of the  $y$ -component form drag  $(H^{-1} \overline{f v'_1 h'_1})$  is created by the eddy thickness flux in the onshore direction  $(\overline{v'_1 h'_1})$ . Baroclinic instability is flattening the isopycnal between the overflow and the upper layer by making the upper-layer flux thickness up the slope, while making the overflow layer flux thickness down the slope, which confirms that baroclinic instability is what generates the eddies in the upper layer and induces the double-gyre eddy-driven topographic  $\beta$  plume there.

*d. The time-mean flow field of the overflow layer*

The overflow layer shows a descent at the rate of 0.2 near the strait (Fig. 6d). This rate exceeds that of the frictional Ekman number  $\nu/f$ , 0.1, and indicates that the overflow is losing its momentum to something other than bottom friction, which we will show to be the upper layer. This increase in the rate of descent is observed

only near the strait. The overflow layer is roughly descending at the rate of the frictional Ekman number away from the strait.

**WHY DOES THE OVERFLOW DESCEND SHARPLY NEAR THE STRAIT?**

If the overflow layer does not interact with the upper layer, its energy loss is solely due to bottom friction but, when the overflow interacts with the upper layer, it can also lose energy to the upper layer. Here, the energy balance of the overflow is examined so as to understand why the overflow descends at a larger rate near the strait compared to its rate farther downstream. The energy balance equation of the overflow layer can be derived from the overflow momentum equations:

$$\frac{\partial(\text{KE} + \text{PE})}{\partial t} + \nabla \cdot [\text{KE} + g'h_2(h_2 - D)]\mathbf{u}_2 = -\mathbf{U}_2 \cdot \nabla p_1 - 2\nu\text{KE}, \tag{6}$$

where KE is the kinetic energy defined as

$$\text{KE} = \frac{h_2}{2} (u_2^2 + v_2^2) \tag{7}$$

and PE is the potential energy defined as

$$PE = \int_{-D}^{h_2-D} g'z dz = \frac{1}{2}g'h_2(h_2 - 2D) : \quad (8)$$

$D$  is the bottom topography depth. Since Eq. (6) is an energy balance equation at a point, an energy balance equation of each cross section in the across-slope direction ( $x$  direction) is derived to see how the overflow energy balance evolves downstream from the strait. Taking a time average and across-slope integration to Eq. (6),

$$\overline{\int_{-A}^A dx \nabla \cdot [\text{KE} + g'h_2(h_2 - D)] \mathbf{u}_2} = - \overline{\int_{-A}^A dx h_2 \mathbf{u}_2 \cdot \nabla p_1} - 2\nu \overline{\int_{-A}^A \text{KE} dx} \quad (9)$$

in which  $x = A, -A$  is where the time-mean overflow-layer thickness is zero (Fig. 10a). The lhs is a sum of the divergence of kinetic energy flux and the pressure work to the overflow layer due to the interface tilt. The latter term is basically the potential energy term for the overflow layer. The rhs is a sum of form drag and dissipation, which will extract energy from the overflow layer (Fig. 10a).

The energy balance of the overflow layer [Eq. (9)] shows that the overflow loses its energy to both form drag and dissipation and that both of these terms are of the same order close to the strait (Fig. 10). The form drag term shows its negative maximum close to where the negative maximum of form drag is located (Fig. 9d) and where a steep angle of descent is observed in the time mean (Fig. 6d). Because the upper layer extracted energy out of the overflow at a rate similar to bottom friction, the overflow descends at a rate two times larger (0.2) than the frictional Ekman number (0.1). Farther downstream from the strait the potential energy loss is mostly by dissipation, and the cross-isopycnal energy flux is negligible.

The descent of overflows has traditionally been tied as the role of bottom friction and the bottom boundary layer. The steady solution does, indeed, show the gradual broadening of the overflow layer as it slides down the slope with the downslope side descending at a steeper angle than the upslope side, matching the results of Condie (1995) and Wåhlin and Walin (2001). Killworth (2001) hypothesized that the turbulent bottom boundary layer will enhance the rate of descent from that of the bottom Ekman number and make the rate of descent of overflows independent of detailed thermodynamics, entrainment or detrainment, and bottom friction based on the assumption of quadratic drag and local turbulent equilibrium. This assumption of local

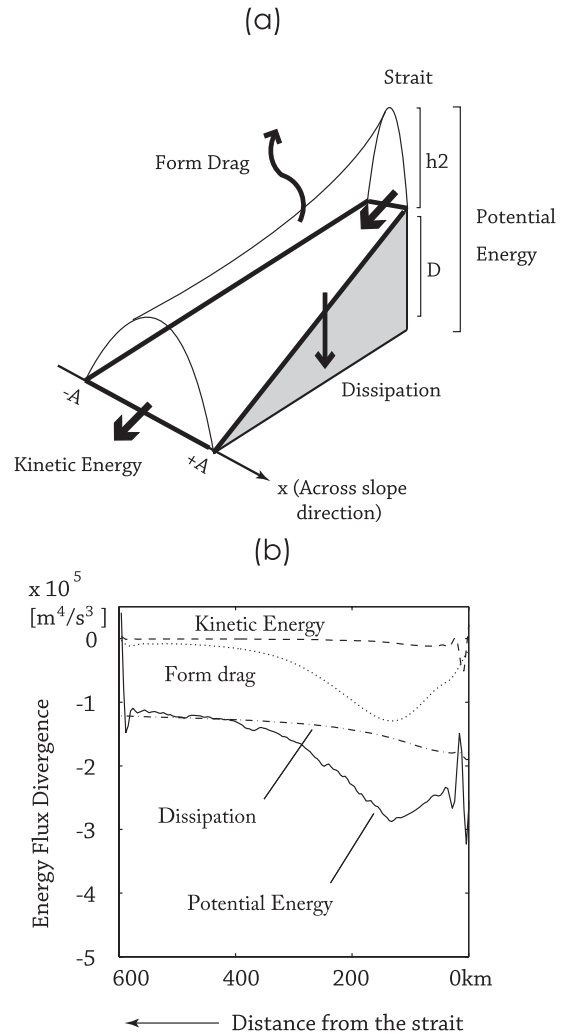


FIG. 10. (a) A schematic of the energy balance for the overflow layer: the overflow comes in the continental slope region with kinetic energy of  $1/2 h_2 (u_2^2 + v_2^2)$  and potential energy of  $1/2 g' h_2 (h_2 - 2D)$ , where  $D$  is the bottom topography depth. As the overflow descends the continental slope, part of this energy is lost to form drag (to the upper layer) and dissipation. The overflow layer is assumed to intersect with the bottom bathymetry at  $x = -A$  and  $A$ . (b) Energy balance of the overflow layer from the strait to the western boundary wall [Eq. (9)]: Energy loss mostly occurs in potential energy (solid line), not kinetic energy (dashed line). Potential energy is lost solely due to dissipation (dashed-dotted line) far from the strait but is a sum of dissipation and form drag (dotted line) near the strait. Form drag has a negative maximum about 150 km downstream from the strait and its magnitude is comparable to dissipation.

turbulent equilibrium, however, does not include the impact of baroclinic instability that varies spatially. While our two-layer model is insufficient to test the hypothesis of Killworth in detail, our model results suggest that eddies due to baroclinic instability between the overflow and the upper ocean can be an additional

energy sink for overflows to what Killworth suggested. As the energy balance of the overflow in our model shows, the upper layer is a nonnegligible energy sink for the overflow layer (Fig. 10).

The integrated energy balance of the overflow from the strait can also be roughly diagnosed by examining the distance of descent. By the time the overflow reaches the western wall, the maximum thickness of the overflow layer has descent about 100 km offshore from the strait (Fig. 6d). The frictional Ekman number estimates a descent over about 70 km, so the remaining 30 km is likely due to energy lost to the upper layer. Thus, 30% of the total descent is due to the energy transfer to the upper layer, while 70% is due to bottom friction. The integrated energy balance also shows that the energy flux to the upper layer is smaller compared to bottom friction but still on the same order. The role of eddies playing a significant role on the descent of overflow matches the model result of Ezer (2005) in which 30% of overflow descent was attributed to bottom friction and the rest to other processes. Although the ratio attributed to bottom friction is not the same as ours, their result supports that overflows descend not only by bottom friction but by other processes as well, and we suspect that the eddies play a significant part.

### 5. The full topographic $\beta$ plume: Revisiting Case 1

Flow fields for Case 1 (Figs. 3a–d) are now examined by comparing them to those for Cases 2 and 3. A snapshot of the sea surface height (Fig. 3a) is qualitatively similar to that in Case 3 (Fig. 6a). Strong cyclonic and anticyclonic eddies are observed with characteristics similar to those in Case 3, which suggests that the eddies observed in Case 1 formed through baroclinic instability. A noticeable difference from Case 3 is the tendency of having more cyclonic eddies than anticyclonic eddies. This tendency is likely the effect of entrainment since entrainment drives a cyclonic circulation in the upper layer as shown in Case 2.

A snapshot of the overflow layer thickness (Fig. 3b) is also similar to that in Case 3 (Fig. 6b). Anticyclonic eddies form close to the strait but compared to Case 3, these eddies are thicker and more energetic and are flowing along the continental slope over a longer distance while keeping their original thickness. These differences are likely the effect of entrainment because entrainment adds mass and induces anticyclonic motion through vortex squashing.

#### a. The time-mean flow: The PV balance

The time mean of the sea surface height shows a formation of a cyclonic topographic  $\beta$  plume with a

transport of 4.1 Sv along bathymetric contours (Fig. 3c). This cyclonic circulation is analogous to the entrainment-driven topographic  $\beta$  plume observed in Case 2 (Fig. 5a). Although eddies are dominant in the snapshot flow field, the time-mean flow shows that the cyclonic topographic  $\beta$  plume forced by entrainment is still present and is a robust feature. Close to the strait, however, there is an anticyclonic circulation with a transport of 1.3 Sv in the onshore side of the cyclonic topographic  $\beta$  plume. The transport of this anticyclonic circulation is not as strong as the cyclonic gyre but is comparable to the overflow transport. As a result, the circulation close to the strait has a double-gyre structure rather than a single gyre, which is the character of the eddy-driven topographic  $\beta$  plume observed in Case 3 (Fig. 6c). The eddies appear to have an effect on the time-mean flow of the upper layer close to the strait.

The time mean of the overflow layer thickness shows that the overflow descends at a sharper angle near the strait than farther downstream from the strait (Fig. 3d). This feature is analogous to that observed in Case 3 (Fig. 6d), which suggests that baroclinic instability is likely its cause. Baroclinic instability is transferring momentum and energy of the overflow layer to the upper layer near the strait and thus enhancing the descent of the overflow compared to the frictional Ekman number.

The time-mean flow field of the upper layer shows characteristics of both the diabatic and eddy-driven topographic  $\beta$  plume. Then, how has the PV balance changed from that of Cases 2 and 3? The PV balance in the entrainment region shows PV forcing by entrainment ( $qw^*$ ) and eddy PV flux divergence ( $-\nabla \cdot \mathbf{U}'q'$ ) on the same order (Fig. 11). The role of eddies is to create a positive total PV forcing region (sum of PV forcing by entrainment and eddy PV flux divergence) on the offshore side of the entrainment region while creating a negative PV forcing region on the onshore side. As a result, a double-gyre topographic  $\beta$  plume, which is a typical characteristic of the eddy-driven topographic  $\beta$  plume, forms in the time-mean flow field near the strait (Fig. 12).

To examine how well the linear vorticity balance [Eq. (1)] estimates the transport of the cyclonic part of the topographic  $\beta$  plume in the presence of eddies, the magnitude of entrainment is varied while its location is kept fixed (Fig. 13). The transport of the cyclonic topographic  $\beta$  plume is like that of Case 3 when entrainment is zero. As the magnitude of entrainment increases, the transport of the cyclonic topographic  $\beta$  plume increases and eventually approaches values close to the linear estimate [Eq. (1)]. Entrainment works as a drag on the overflow layer, so an increase in entrainment likely reduces the magnitude of momentum transfer from the overflow to the upper layer due

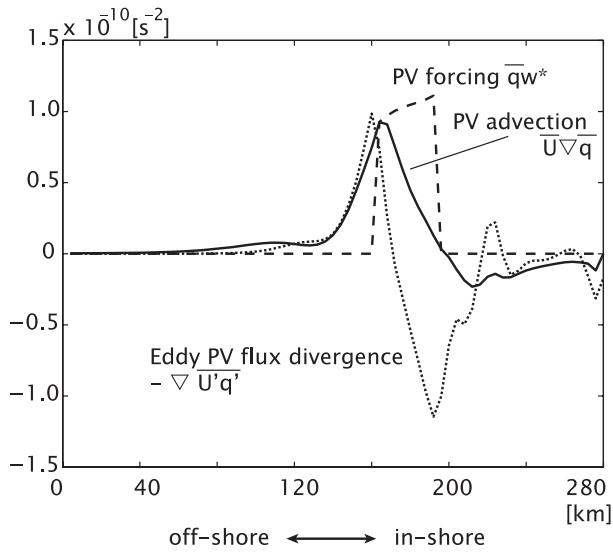


FIG. 11. PV balance at the entrainment region: Mean PV advection (solid line,  $\overline{\mathbf{U}} \cdot \nabla \bar{q}$ ) is balanced by the PV forcing (dotted line;  $\overline{q}w^*$ ) and the eddy PV flux divergence (dashed line,  $-\nabla \cdot \overline{\mathbf{U}'q'}$ ). Notice that the eddy PV flux divergence is creating a negative PV advection region that leads to the double-gyre topographic  $\beta$  plume.

to baroclinic instability compared to the case with no entrainment. The entrainment-driven topographic  $\beta$  plume, therefore, starts to overwhelm the eddy-driven topographic  $\beta$  plume as entrainment increases. The observed transport is 0.5–1.0 Sv more than the linear estimate but, roughly speaking, the linear vorticity balance estimates the transport well. The eddies are

strong enough to modify the structure of the total PV forcing region but not to enhance its magnitude significantly. Note that the mean background PV gradient in the upper layer, which is used for the linear estimate, is now different from that used in Case 2 because the overflow layer exists. The upper layer thickness gradient that is dominantly controlling the background PV gradient is now larger than the slope. So the linear estimate of the transport in the cyclonic topographic  $\beta$  plume is less than the value calculated in Case 2 (Fig. 5).

*b. Comparing with observations and other numerical models*

Baroclinic instability between the overflow and the upper layer is a plausible mechanism that can explain the formation of eddies and the time variability observed in the Mediterranean and Faroe Bank Channel overflow.

The size and magnitude of the cyclonic eddies observed in Case 1 are analogous to those observed near the Faroe Bank Channel from satellite altimetry (Ezer 2006). The eddies are also analogous to those observed at the surface of the Gulf of Cadiz along with anticyclonic meddies below (Carton et al. 2002). Whether the cyclonic eddies outnumber the anticyclonic eddies remains unclear, but observations support, or at least do not oppose, the results of our numerical model. Past numerical models, including DOME experiments, support the formation of these eddies (Jiang and Garwood 1996; Jungclaus et al. 2001; Ezer 2006) with the vorticity balance also showing the importance of eddies (Ezer 2005).

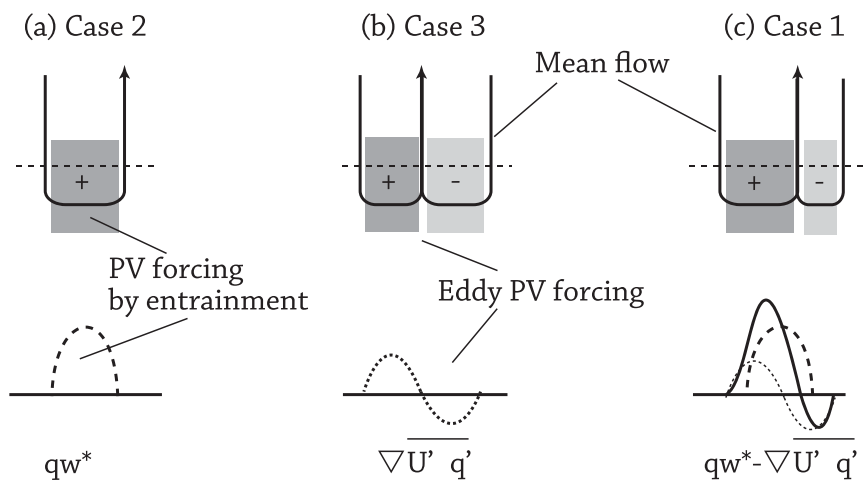


FIG. 12. Schematic showing the characters of the PV balance near the entrainment region for (a) Case 2, (b) Case 3, and (c) Case 1. The figures at the top show the bird's-eye view of the PV balance and the direction of the mean flow. The figures at the bottom show the cross-sectional (dotted line in the top three figures) view of the total PV forcing that is balancing the mean PV advection.

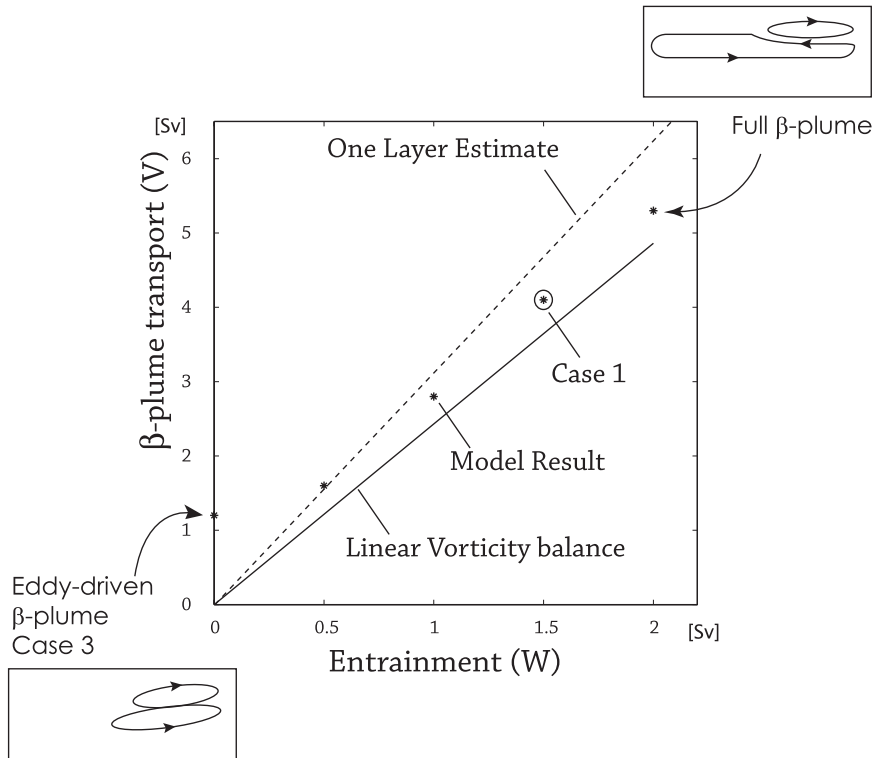


FIG. 13. Transport of the topographic  $\beta$  plume as a function of entrainment ( $W$ ):  $W = 0$  corresponds to Case 3 and  $W = 1.5$  Sv corresponds to Case 1 (circle). The transport of the topographic  $\beta$  plume increases (asterisks) as  $W$  increases and the values also become closer to the linear estimate (solid line). The transport of the model results are slightly greater than the linear estimate by 0.5–1.0 Sv, which is likely a result of the eddies. Note that the linear estimate shown here is a smaller estimate than used for Case 2 (dotted line) because the mean PV gradient of the upper layer near the strait has increased in the presence of the overflow layer.

The time series of the overflow layer thickness in Case 1 shows fluctuation from 0 to 150 m in about 4-days downstream from the strait (Fig. 14). This feature is analogous to that observed for the Faroe Bank Channel overflow in temperature (Fig. 2; Høyer and Quadfasel 2001). This chain of eddies was also observed in models using more realistic bathymetry even when the transport in the strait is steady (Ezer 2006; Riemenschneider and Legg 2007). When the numerical model is set close to the parameter space of the Mediterranean overflow, the overflow layer showed a fluctuation of 7–8-day period, which is also similar to that observed (Chérubin et al. 2003; Kida et al. 2008). Although the longer period observed for the Mediterranean overflow may be due to many differences that exist between the two overflows, the model results suggest that the difference is due to smaller  $f$  ( $8.5 \times 10^{-5} \text{ s}^{-1}$ ) compared to the Faroe Bank Channel, higher latitude, overflow ( $f = 1.4 \times 10^{-4} \text{ s}^{-1}$ ).

Because baroclinic instability occurs locally near the strait, it creates a region of large sea surface height variability close to the strait (Fig. 15). This feature is

analogous to that observed downstream of the Faroe Bank Channel, Mediterranean, and Denmark Strait overflow from satellite altimetry (Høyer and Quadfasel 2001; Høyer et al. 2002). A region of large sea surface height variability could be a product of other processes, but the fact that similar features are observed near three major overflows indicates that the feature is connected to the dynamics of the overflow and that baroclinic instability is a plausible mechanism for creating such a feature.

There is some evidence that a time-mean cyclonic circulation exists in the upper oceanic layer above overflows. The time-mean circulation of the Northern Atlantic at 400-m depth observed from subsurface floats (Lavender et al. 2005) shows a cyclonic circulation above the Faroe Bank Channel overflow. Although this observed cyclonic circulation may be part of a rim current of the cyclonic subpolar gyre, the magnitude of the sea surface height gradient is of the same order as the topographic  $\beta$  plume simulated in the upper layer in Case 1 (Fig. 3a). Mauritzen et al. (2001) also show that a

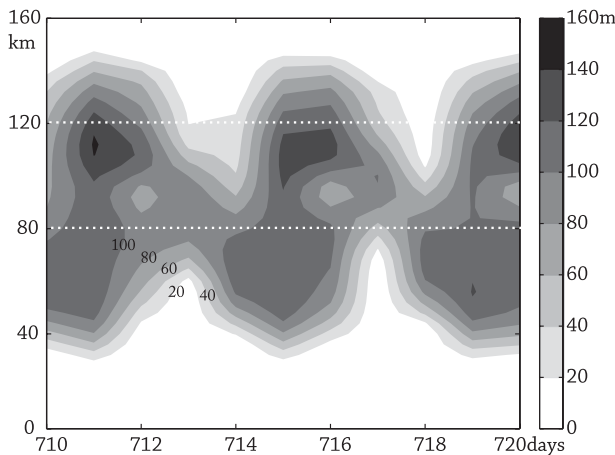


FIG. 14. Time series of the overflow layer thickness in the across-slope direction for Case 1, observed 140 km downstream from the strait. The thickness fluctuates between 0 and 150 m at 4–5-day period. The region between the two dotted lines corresponds to the size in Fig. 2.

cyclonic circulation is likely to exist above the Mediterranean overflow from current meters. The anticyclonic topographic  $\beta$  plume in Case 1 or 3 may be too weak and too small to compare with present available observation data, but high-resolution numerical models do appear to create such circulations (Peliz et al. 2007).

## 6. Summary and remarks

In the introductory section, we raised three specific questions regarding the interactions between a marginal sea overflow and the upper ocean, and here we summarize our response.

- 1) *How does the upper oceanic layer balance the mass loss caused by entrainment into an overflow?* The mass sink within the upper ocean implies a convergent flow and vortex stretching. The result in the upper ocean is a cyclonic topographic  $\beta$  plume that is oriented along bathymetric contours. The background topographic  $\beta$  has a dominant control over this circulation in terms of its transport and its structure. The transport of this circulation is larger than that required by entrainment, and the linear vorticity balance gives a reasonable estimate of this transport.
- 2) *What is the primary mechanism of eddy variability in the overflow and its overlying layers?* Baroclinic instability is likely the main process that generates eddy variability that extends through the overflow and the upper ocean. The PV balance diagnosed from numerical simulations indicates that eddy fluxes between layers are likely to be most important near the strait (within  $\sim 100$  km) where the

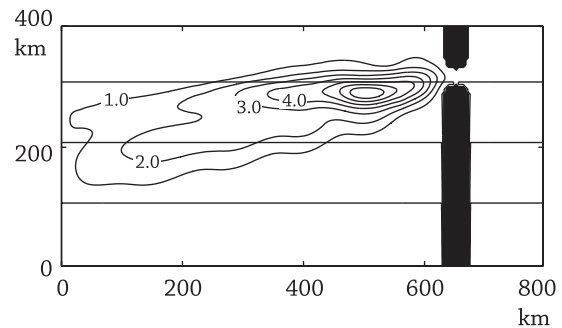


FIG. 15. Rms of sea surface height variability for Case 1, contoured from 0 to 7 cm every 1 cm: High variability is observed near the strait with a maximum of about 7 cm.

baroclinic instability is growing most rapidly. The eddy variability persists farther downstream but is not growing, so it is not associated with a significant vertical flux of momentum or energy.

- 3) *Do eddies created by baroclinic instability affect the overflow and the upper ocean in the time mean?* For our choice of inflow and entrainment parameters, the presence of eddies enhances the transport of the cyclonic topographic  $\beta$  plume within the upper layer only slightly. However, the PV balance near the entrainment region changes from a linear vorticity balance to a turbulent Sverdrup balance. The structure of the time-mean circulation also shows the character of the eddy-driven topographic  $\beta$  plume—cyclonic and anticyclonic gyres offshore and inshore, respectively—rather than an entrainment-driven, single-gyre, topographic  $\beta$  plume. Because a growing instability process transfers momentum from the overflow to the upper layer, the overflow layer descends the topographic slope somewhat more steeply than would occur by bottom friction alone.

As far as the formation of eddies is concerned, the growth rate of baroclinic instability is the important controlling parameter. But, an a priori estimate of eddy contribution to the descent of overflows requires an estimate of the magnitude of eddy PV fluxes, which is a subject of intense research and somewhat beyond the scope of this paper (see, e.g., Gent and McWilliams 1990; Visbeck et al. 1997). Assessing the role of eddies in the descent of overflows in numerical models requires careful consideration and treatment of the bottom and lateral friction used in numerical models. Eddies will be suppressed when a large bottom friction parameter, such as used in low-resolution climate models (Nakano and Sugimotohara 2002), is used. For example, some numerical tests showed that overflows in high-resolution and low-resolution models have a similar angle of descent even though the eddy intensities are drastically

different. It was speculated that the descent in low-resolution models was enhanced by a large vertical friction (Legg et al. 2006). Suppression of eddies in descending overflows is also observed when horizontal viscosity increases (Ezer and Mellor 2004). In our numerical experiments, the strength of eddies and entrainment was independently controlled, but these two processes may very well interact with each other in more complete numerical models or in the real ocean and affect the descent of overflows. If baroclinic instability enhances entrainment, for example, it would decrease  $g'$  and the magnitude of interfacial form drag, therefore diminishing the effect of eddies on the descent of overflows. But, on the other hand, enhanced entrainment will also act as a brake on the overflow layer because the newly incorporated upper-layer water mass has significantly less (downstream) momentum than in the overflow. Examining how interaction of entrainment and baroclinic eddies affects overflows requires further research using more realistic (less constrained and less idealized) numerical models than applied here.

The idealized model used in this study neglected all but the largest scales of spatial variability of bottom topography. Bottom topographic features like canyons and ridges can induce bottom form drag that, according to Özgökmen et al. (2003), can be comparable or even greater than momentum drag caused by bottom friction alone. The significance of bottom form drag can be estimated from the energy balance equation, Eq. (9). By taking the depth of the slope as  $D = D_o + d$ , where  $D_o$  is the constant slope and  $d$  the perturbation, the pressure work term in Eq. (9) can be rewritten as

$$\begin{aligned} \nabla \cdot \overline{g'h_2(h_2 - D)\mathbf{u}_2} &= \nabla \cdot \overline{g'h_2(h_2 - D_o)\mathbf{u}_2} - \nabla \cdot \overline{g'h_2d\mathbf{u}_2} \\ &= \nabla \cdot \overline{g'h_2(h_2 - D_o)\mathbf{u}_2} - \overline{h_2\mathbf{u}_2} \cdot \overline{g'\nabla d}, \end{aligned} \quad (10)$$

where the second term on the rhs is the bottom form drag term. The significance of this bottom form drag compared to the interfacial form drag term,  $\overline{h_2\mathbf{u}_2} \cdot \nabla p_1$ , can be estimated by taking the ratio of the two:

$$\frac{g'\delta d}{g\delta\eta},$$

where  $\nabla p_1$  is scaled using the sea surface height variability  $\delta\eta$  and the topographic variability scale is taken as  $\delta d$ . In Case 3,  $\delta\eta$  is about 5 cm, so for the bottom form drag to be roughly the same magnitude as the interfacial form drag (ratio  $\simeq 1$ ),  $\delta d$  needs to be about 100 m. For the Faroe Bank Channel overflow, small-scale changes in bathymetry  $O(100 \text{ m})$  are not observed near the strait, so we suspect that the effect of bottom form drag

is not  $O(1)$ . For the Mediterranean overflow, however, canyons with depth changes of 100 m do exist, and numerical experiments by Wåhlin (2002) support bathymetry changes as the leading cause for the bifurcation of the Mediterranean overflow observed at Portimão Canyon.

This paper has emphasized the Faroe Bank Channel overflow because we think that it is likely to present the most prominent example of strong eddy-driven interaction between an overflow and the upper layer. The Denmark Strait has roughly similar transports, depths, and bottom slope, but differs in that it is at the western boundary of a subpolar basin. The upper-layer circulation induced by the overflow is likely to be overwhelmed by the even stronger time-varying western boundary current (East Greenland Current). The Mediterranean overflow appears to develop some eddy variability in its overlying oceanic layer, but the region may be too shallow compared to the Faroe Bank Channel for the eddy-driven topographic  $\beta$  plume to have a significant transport [see Eq. (1)]. Smaller upper ocean thickness leads to stronger background PV gradient and thus smaller transport of the eddy-driven topographic  $\beta$ -plume transport [Eq. (4)]. The entrainment of the Mediterranean overflow is comparable to that of the Faroe Bank Channel overflow (Price and Baringer 1994), so the entrainment-driven topographic  $\beta$  plume is likely to overwhelm the eddy-driven topographic  $\beta$  plume. Because of its presence on the eastern boundary, the topographic  $\beta$  plume of the Mediterranean overflow may connect to the Atlantic and establish a basin-scale circulation and form the driving mechanism for the Azores Current (Jia 2000; Özgökmen et al. 2001; Kida et al. 2008). Knowing that topographic  $\beta$  plumes are likely consequences for overflows may lead to a better understanding of regional circulations.

*Acknowledgments.* The authors thank Drs. Karl Helfrich, Sonya Legg, Amy Bower, Raffael Ferrari, and two anonymous reviewers for many useful comments. We are also grateful to Dr. Bob Hallberg of NOAA/GFDL for allowing us to use his isopycnal coordinate model, HIM. SK's support during the time of his Ph.D. research in the MIT/WHOI Joint Program was provided by the National Science Foundation through Grant OCE04-24741. JP and JY have also received support from the Climate Process Team on Gravity Current Entrainment, NSF Grant OCE-0611530. JY has also been supported by NSF Grant OCE-0351055.

#### REFERENCES

- Borenäs, K., and P. Lundberg, 2004: The Faroe-Bank Channel deep-water overflow. *Deep-Sea Res. II*, **51**, 335–350.

- Bruce, J. G., 1995: Eddies southwest of the Denmark Strait. *Deep-Sea Res. I*, **42**, 13–29.
- Candela, J., 2001: Mediterranean water and global circulation. *Ocean Circulation and Climate*, G. Siedler et al., Eds., Elsevier, 419–429.
- Carton, X., L. Chérubin, J. Paillet, Y. Morel, A. Serpette, and B. L. Cann, 2002: Meddy coupling with a deep cyclone in the Gulf of Cadiz. *J. Mar. Syst.*, **32**, 13–42.
- Cenedese, C., J. A. Whitehead, T. A. Ascarelli, and M. Ohiwa, 2004: A dense current flowing down a sloping bottom in a rotating fluid. *J. Phys. Oceanogr.*, **34**, 188–203.
- Chérubin, L. M., N. Serra, and I. Ambar, 2003: Low-frequency variability of the Mediterranean undercurrent downstream of Portimão Canyon. *J. Geophys. Res.*, **108**, 3058, doi:10.1029/2001JC001229.
- Choboter, P. F., and G. E. Swaters, 2000: On the baroclinic instability of axisymmetric rotating gravity currents with bottom slope. *J. Fluid Mech.*, **408**, 149–177.
- Condie, S. A., 1995: Descent of dense water masses along continental slopes. *J. Mar. Res.*, **53**, 897–928.
- Etling, D., F. Gelhardt, U. Schrader, F. Brennecke, G. Kuhn, G. C. d'Hieres, and H. Didelle, 2000: Experiments with density currents on a sloping bottom in a rotating fluid. *Dyn. Atmos. Oceans*, **31**, 139–164.
- Ezer, T., 2005: Entrainment, diapycnal mixing and transport in three-dimensional bottom gravity current simulations using the Mellor–Yamada turbulence scheme. *Ocean Modell.*, **9**, 151–168.
- , 2006: Topographic influence on overflow dynamics: Idealized numerical simulations and the Faroe Bank Channel overflow. *J. Geophys. Res.*, **111**, C02002, doi:10.1029/2005JC003195.
- , and G. L. Mellor, 2004: A generalized coordinate ocean model and a comparison of the bottom boundary layer dynamics in terrain-following and in  $z$ -level grids. *Ocean Modell.*, **6**, 379–403.
- Gent, P., and J. McWilliams, 1990: Isopycnal mixing in ocean circulation models. *J. Phys. Oceanogr.*, **20**, 150–155.
- Geyer, F., S. Østerhus, B. Hnassen, and D. Quadfasel, 2006: Observations of highly regular oscillations in the overflow plume downstream of the Faroe Bank Channel. *J. Geophys. Res.*, **111**, C12020, doi:10.1029/2006JC003693.
- Haidvogel, D. B., and P. B. Rhines, 1983: Waves and circulation driven by oscillatory winds in an idealized ocean basin. *Geophys. Astrophys. Fluid Dyn.*, **25**, 1–63.
- Hallberg, R., 1997: Stable split time stepping schemes for large-scale ocean modeling. *J. Comput. Phys.*, **135**, 54–65.
- Helfrich, K. R., 2006: Nonlinear adjustment of a localized layer of buoyant, uniform, potential vorticity fluid against a vertical wall. *Dyn. Atmos. Oceans*, **41**, 149–171.
- Høyer, J. L., and D. Quadfasel, 2001: Detection of deep overflows by satellite altimetry. *Geophys. Res. Lett.*, **28**, 1611–1614.
- , —, and O. B. Anderson, 2002: Deep ocean currents detected with satellite altimetry. *Can. J. Remote Sens.*, **28**, 556–566.
- Jia, Y., 2000: The formation of an Azores Current due to Mediterranean overflow in a modeling study of the North Atlantic. *J. Phys. Oceanogr.*, **30**, 2342–2358.
- Jiang, L., and R. W. Garwood, 1996: Three-dimensional simulations of overflows on continental slopes. *J. Phys. Oceanogr.*, **26**, 1214–1233.
- Jungclauss, J. H., J. Hauser, and R. H. Käse, 2001: Cyclogenesis in the Denmark Strait overflow plume. *J. Phys. Oceanogr.*, **31**, 3214–3229.
- Käse, R. H., J. B. Girton, and T. B. Sanford, 2003: Structure and variability of the Denmark Strait Overflow: Model and observations. *J. Geophys. Res.*, **108**, 3181, doi:10.1029/2002JC001548.
- Kida, S., J. F. Price, and J. Yang, 2008: The upper-oceanic response to overflows: A mechanism for the Azores Current. *J. Phys. Oceanogr.*, **38**, 880–895.
- Killworth, P. D., 1977: Mixing on the Weddel Sea continental slope. *Deep-Sea Res.*, **24**, 427–448.
- , 2001: On the rate of descent of overflows. *J. Geophys. Res.*, **106**, 22 267–22 275.
- Krauss, W., and R. H. Käse, 1998: Eddy formation in the Denmark Strait overflow. *J. Geophys. Res.*, **103**, 15 525–15 538.
- Lavender, K. L., W. B. Owens, and R. E. Davis, 2005: The mid-depth circulation of the subpolar North Atlantic Ocean as measured by subsurface floats. *Deep-Sea Res. I*, **52**, 767–785.
- Legg, S., R. W. Hallberg, and J. B. Girton, 2006: Comparison of entrainment in overflows simulated by  $z$ -coordinate, isopycnal and non-hydrostatic models. *Ocean Modell.*, **10**, 69–97.
- Mauritzen, C., Y. Morel, and J. Paillet, 2001: On the influence of Mediterranean water on the central waters of the North Atlantic Ocean. *Deep-Sea Res. I*, **48**, 347–381.
- , J. Price, T. Sanford, and D. Torres, 2005: Circulation and mixing in the Faroese Channels. *Deep-Sea Res. I*, **52**, 883–913.
- Nakano, H., and N. Suginoara, 2002: Effects of bottom boundary layer parameterization on reproducing deep and bottom waters in a World Ocean Model. *J. Phys. Oceanogr.*, **32**, 1209–1227.
- Nof, D., 1991: Lenses generated by intermittent currents. *Deep-Sea Res. I*, **38**, 325–345.
- , N. Paldor, and S. Van Gorder, 2002: The Reddy maker. *Deep-Sea Res. I*, **49**, 1531–1549.
- Özgökmen, T. M., E. P. Chassignet, and C. G. H. Rooth, 2001: On the connection between the Mediterranean Outflow and the Azores Current. *J. Phys. Oceanogr.*, **31**, 461–480.
- , W. E. Johns, H. Peters, and S. Matt, 2003: Turbulent mixing in the Red Sea outflow plume from a high-resolution non-hydrostatic model. *J. Phys. Oceanogr.*, **33**, 1846–1869.
- Peliz, A., J. Dubert, P. Marchesiello, and A. Teles-Machado, 2007: Surface circulation in the Gulf of Cadiz: Model and mean flow structure. *J. Geophys. Res.*, **112**, C11015, doi:10.1029/2007JC004159.
- Plumb, R. A., 1986: Three-dimensional propagation of transient quasi-geostrophic eddies and its relationship with the eddy forcing of the time-mean flow. *J. Atmos. Sci.*, **43**, 1657–1678.
- Price, J. F., and M. O. Baringer, 1994: Outflows and deep water production by marginal seas. *Prog. Oceanogr.*, **33**, 161–200.
- Rhines, P. B., and W. R. Holland, 1979: A theoretical discussion of eddy-driven mean flows. *Dyn. Atmos. Oceans*, **3**, 289–325.
- Riemenschneider, U., and S. Legg, 2007: Regional simulations of the Faroe Bank Channel overflow in a level model. *Ocean Modell.*, **17**, 93–122.
- Saunders, P. M., 2001: The dense northern overflows. *Ocean Circulation and Climate*, G. Siedler et al., Eds., Elsevier, 401–417.
- Smith, P. C., 1975: A streamtube model for bottom boundary currents in the ocean. *Deep-Sea Res.*, **22**, 853–873.
- Spall, M. A., 2000: Buoyancy-forced circulations around islands and ridges. *J. Mar. Res.*, **58**, 957–982.
- , and J. F. Price, 1998: Mesoscale variability in Denmark Strait: The PV outflow hypothesis. *J. Phys. Oceanogr.*, **28**, 1598–1623.



- Stanton, B. R., 1983: Low frequency variability in the Mediterranean Undercurrent. *Deep-Sea Res. II*, **30**, 743–761.
- Stommel, H. M., 1982: Is the South Pacific Helium-3 plume dynamically active? *Earth Planet. Sci. Lett.*, **61**, 63–67.
- Swaters, G. E., 1991: On the baroclinic instability of cold-core coupled density fronts on a sloping continental shelf. *J. Fluid Mech.*, **224**, 361–382.
- Visbeck, M., J. Marshall, T. Haine, and M. Spall, 1997: Specification of eddy transfer coefficients in coarse-resolution ocean circulation models. *J. Phys. Oceanogr.*, **27**, 381–402.
- Wählin, A. K., 2002: Topographic steering of dense currents with application to submarine canyons. *Deep-Sea Res. I*, **49**, 305–320.
- , and G. Walin, 2001: Downward migration of dense bottom currents. *Environ. Fluid Mech.*, **1**, 257–279.
- Warren, B. A., 1981: *Evolution of Physical Oceanography: Scientific Surveys in Honor of Henry Stommel*. The MIT Press, 623 pp.
- Whitehead, J. A., M. E. Stern, G. R. Flierl, and B. A. Klinger, 1990: Experimental observations of baroclinic eddies on a sloping bottom. *J. Geophys. Res.*, **95**, 9585–9610.